JACS
JOURNAL OF THE AMERICAN CHEMICAL SOCIETY
pubs.acs.org/JACS
Article

Bright, Modular, and Switchable Near-Infrared II Emission from Compact Tetrathiafulvalene-Based Diradicaloid Complexes

Lauren E. McNamara, Jan-Niklas Boyn, Christopher Melnychuk, Sophie W. Anferov, David A. Mazziotti, Richard D. Schaller, and John S. Anderson*

Cite This: J. Am. Chem. Soc. 2022, 144, 16447−16455
Read Online
ACCESS | Metrics & More | Article Recommendations | Supporting Information

ABSTRACT: Near-infrared (NIR)-emitting molecules are promising candidates for biological sensing and imaging applications; however, many NIR dyes are large conjugated systems which frequently have issues with stability, solubility, and tunability. Here, we report a novel class of compact and tunable fluorescent diradicaloid complexes which are air-, water-, light-, and temperature-stable. These properties arise from a compressed π manifold which promotes an intense ligand-centered $\pi-\pi$ transition in the NIR II (1000−1700 nm) region and which subsequently emits at ∼1200 nm. This emission is among the brightest known for monomolecular lumiphores with deep NIR II (>1100 nm) emission, nearly an order of magnitude brighter than the commercially available NIR II dye IR 26. Furthermore, this fluorescence is electrochemically sensitive, with efficient switching upon addition of redox agents. The brightness, stability, and modularity of this system distinguish it as a promising candidate for the development of new technologies built around NIR emission.

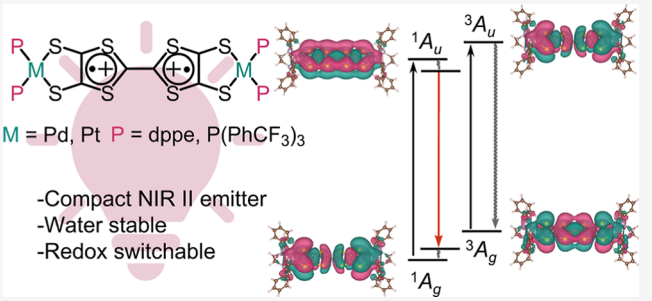

INTRODUCTION

Molecular near-infrared (NIR) dyes and lumiphores have gained recent attention due to their promising applications in biological imaging[1−6] and the development of lasers,[7] detectors,[8] and organic light-emitting diodes.[9] The NIR region (700−1700 nm) falls in the tissue transparent window, so NIR emitters are often implemented for in vivo, in vitro, and intraoperative imaging applications.[1−6,10−12] For these applications, the main challenges facing current NIR dye development are autofluorescence, scattering, and water overtones.[1,13] Both autofluorescence and scattering are dramatically reduced in the NIR II region, but water absorptions at ∼1400 nm pose a significant obstacle for many NIR dyes which frequently have low photoluminescence quantum yields (PLQYs).[1,13]

The physical underpinnings of emission in the NIR region make low PLQYs a considerable challenge facing current molecular dye candidates.[1,10−12,14−16] The PLQYs of organic dyes are empirically found to decrease exponentially with the transition energy, a phenomenon known as the energy gap law.[17,18] For molecular organic NIR dyes, it has been proposed that the associated nonradiative rates are limited by C−H stretching vibrations;[1,17,18] however, large conjugated systems are frequently required to enable low-energy absorption and emission, and eliminating higher-energy vibrational modes (i.e., C−H's) poses significant synthetic difficulties.

These limitations on the PLQY make the development of efficient NIR dyes challenging. Only two NIR dyes, indocyanine green and methylene blue, have been approved by the U.S. FDA, and both emit around 700−800 nm where autofluorescence and scattering can be problematic.[1,2,19−21] In addition to these thiazine and cyanine dyes, donor−acceptor−donor (D−A−D) and polymethine dyes have also been explored to further red-shift the emission into the NIR II region.[22−24] While they are often synthetically challenging, such donor−acceptor and D−A−D systems have recently been successfully employed to synthesize the first organic NIR dyes with emission maxima ≥1200 nm;[25,26] however, these dyes exhibit extremely low PLQYs (≤0.05%). Furthermore, efforts to increase the water solubility of large D−A−D systems often result in dramatically decreased PLQYs in aqueous solution. For example, the first water-soluble D−A−D dye, CH1055-PEG, exhibited ∼20-fold PLQY decrease in water compared to that of the parent compound (CH1055) in toluene.[14]

In addition to D−A−D systems, polymethine dyes are also promising candidates for bright NIR II emission. IR 26 is the brightest commercially available organic dye with an emission maximum ≥1100 nm.[27] While this dye emits around 1130 nm in 1,2-dichloroethane, it still exhibits a limited PLQY (0.05%) due to its low emission energy.[27]

Received: May 10, 2022
Published: August 29, 2022

Aside from poor PLQY values, the scaffold size and complexity required to red-shift the emission into the NIR region poses significant synthetic and solubility challenges.[10−12] The requirement for large conjugated molecular systems makes rational design of stimuli-responsive chromophores, for instance, those that turn on or off in specific chemical or electrochemical environments, extremely challenging.[10−12] Recent progress has been made in the development of compact NIR transition-metal-based emitters; however, these complexes still suffer from low PLQYs at room temperature and in solution.[28−30] It would be advantageous to generate a compact and hence modular organic NIR II-emitting moiety with a high PLQY that could be tuned for some of these responsive applications.

Our laboratory has recently been interested in tetrathiafulvalene-2,3,6,7-tetrathiolate (TTFtt)-bridged bimetallic complexes.[31,32] TTF-based compounds have been studied in semiconducting and conductive materials due to their rich redox and π-stacking properties.[33−39] We have recently discovered facile synthetic methods to install TTFtt between metal centers in unusual redox states which display diradical character.[31,32] In these studies, we noted that doubly oxidized TTF cores have distinct NIR absorbances which arise from comparatively weak C−S π-bonding resulting in a compressed π manifold; however, no photophysical properties beyond absorption spectra have been investigated.[31,32] We wanted to examine whether the synthesis of heavy metal analogues of these complexes could enable NIR emission from this π system.

To test this hypothesis, we have synthesized three novel TTFtt complexes of Pd and Pt. All these complexes display some degree of diradical character. Photophysical measurements reveal extremely bright emission that arises from the unusual geometric and electronic structures of the TTFtt core. This emission is extremely photostable, persists in ambient conditions and aqueous mixtures, and is redox-switchable for several cycles. The stability, tunability, and modularity of these complexes suggest they are promising new candidates for the development of tunable, responsive, and bright NIR dyes.

RESULTS AND DISCUSSION

Synthesis of Novel TTFtt Dications. We accessed the complexes $[\{(dppe)Pd\}_2TTFtt][BAr_4^F]_2$ (**1**), $[\{(dppe)Pt\}_2TTFtt][BAr_4^F]_2$ (**2**), and $[\{((4\text{-}CF_3Ph)_3P)_2Pt\}_2TTFtt][BAr_4^F]_2$ (**3**) via modifications of previously reported procedures (Scheme 1).[32] Transmetalation between phosphine-supported dihalide precursors and the TTFtt synthon $(SnBu_2)_2TTFtt$ followed by in situ oxidation using two equivalents of $[Fc^{BzO}][BAr_4^F]$ [where Fc^{BzO} = benzoylferrocenium, dppe = 1,2-bis(diphenylphosphino)ethane, and BAr_4^F = tetrakis(3,5-bis(trifluoromethyl)phenyl)borate, Scheme 1] provides facile access to **1**, **2**, and **3**. All three dicationic complexes were obtained as crystalline solids in high yields, and single-crystal X-ray diffraction (SXRD) reveals that all three display planar P_2M_2TTFtt geometries with no π-stacking in the solid state (see the Supporting Information). TTF units have a high propensity to π-stack, and we propose that shielding of the TTF core by the large BAr_4^F anions prevents oligomerization. Such shielding is particularly apparent in the structure of **3** where fluorophilic interactions between the capping phosphine ligands and the $[BAr_4^F]^-$ counter anions lead to encapsulation of the dicationic TTFtt core.

Scheme 1. Synthesis of Novel TTFtt Dications

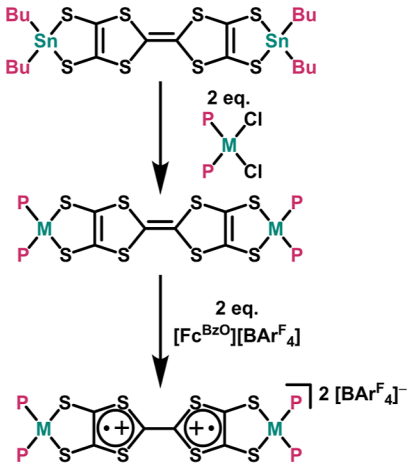

	M	P
1	Pd	dppe
2	Pt	dppe
3	Pt	2 x P(4-CF_3Ph)$_3$

Photophysical Properties. As observed in previous TTFtt dicationic complexes,[31,32] **1**−**3** have intense NIR absorbances at ∼1000 nm, which can be assigned to π−π transitions (Figure 1a). The molar absorptivity of these features is ∼80,000 M^{-1} cm^{-1}. Such strong absorbance is valuable in capturing a larger fraction of incident light to maximize emissive properties.[22] Despite changing metal centers and ligands, these absorbances are nearly superimposable and shift only minimally across analogues. Upon NIR excitation (900 nm), **1**−**3** exhibit intense emission centered at ∼1200 nm. A minimal hypsochromic shift is apparent in the NIR absorption maximum and photoluminescence (PL) spectra of **3** compared to those of **1** and **2**; however, at 77 K, the PL spectrum of **3** aligns with the other analogues (Figure 1b). Interestingly, the excitation spectra of all three complexes display strong vibronic features and nearly identical maxima, with minor variations present at ∼1050 nm (see the Supporting Information). In general, this photophysical data suggests absorption and emission from the TTF core which is remarkably invariant to the identity of the capping metal/ligand combination.

We then performed PLQY measurements across all three analogues. Both **1** and **2** have nearly identical PLQY values of ∼0.14% (see Table 1), whereas **3** has a notably higher PLQY of 0.43%. These quantum yields distinguish this novel class of dyes as among the brightest monomolecular NIR II lumiphores, with **3** measuring nearly an order of magnitude higher than the commercially available NIR II dye IR 26. As mentioned above, the high extinction coefficients of these complexes are also beneficial. Molecular NIR dyes are frequently characterized by a "brightness" which is a product of the extinction coefficient of the absorption times the PLQY.[22] The values obtained for **1**−**3** are ∼10,000−40,000 M^{-1} cm^{-1}, which are again among the best reported, particularly in this spectral region.

Transient absorption (TA) spectra were then acquired for all three complexes to understand the electronic structure responsible for this bright emission (Figure 1c,d,e and Supporting Information). Initially, a broad ground-state bleach is present at ∼1000 nm, with an unusually sharp excited-state

https://doi.org/10.1021/jacs.2c04976
J. Am. Chem. Soc. 2022, 144, 16447−16455

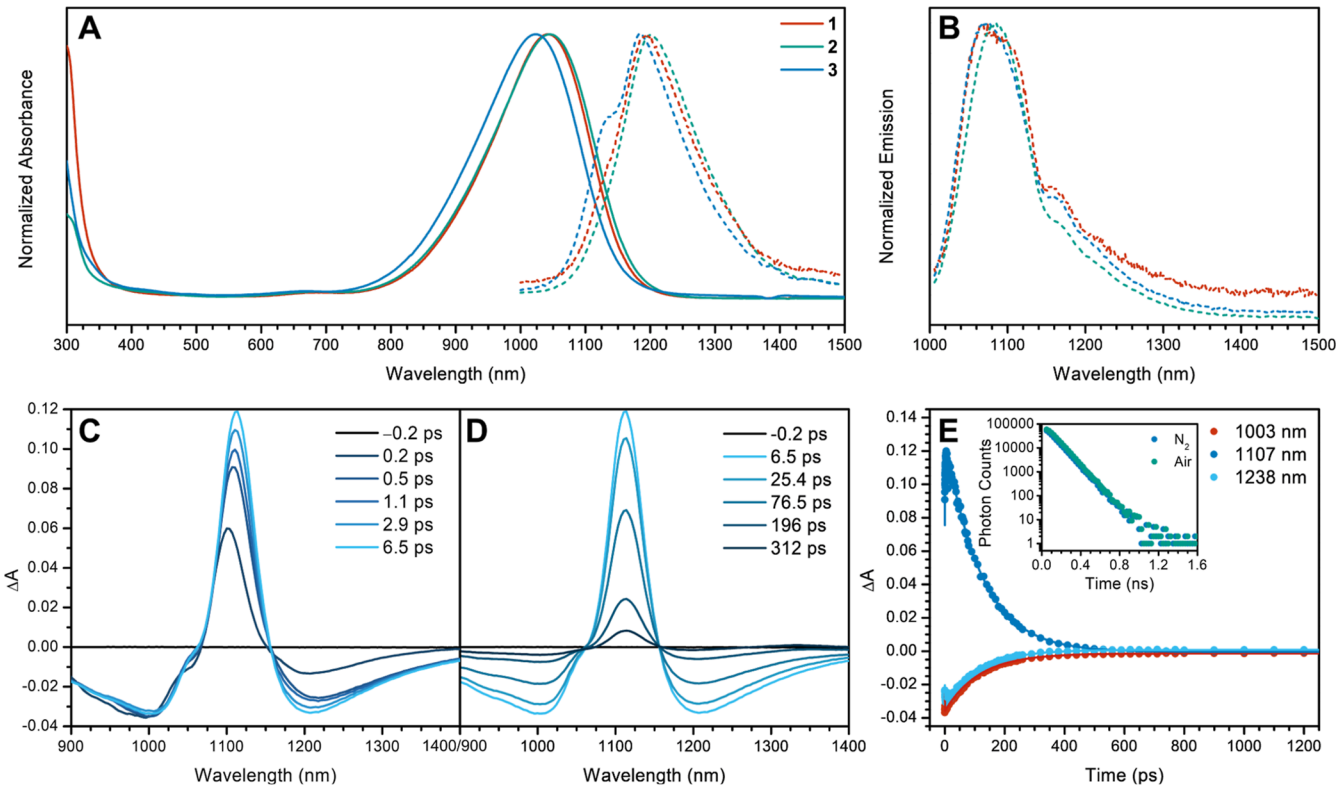

Figure 1. Steady-state and time-resolved photophysical spectra. (a) Normalized UV−vis−NIR (solid) and PL (dashed) spectra of **1**, **2**, and **3** in DCM at 298 K. (b) Normalized PL spectra of **1**, **2**, and **3** in 1:1 DCM/toluene at 77 K. (c) Growth of TA spectra of **3** in DCM at 298 K. (d) Decay of TA spectra of **3** in DCM at 298 K. (e) Transient kinetics of **3** at key wavelengths in DCM at 298 K. Inset: TCSPC data of **3** showing identical lifetimes in air and under N_2.

Table 1. Experimental and Theoretical Photophysical Parameters[a]

	1	2	3
ϕ_{PL}	0.00135	0.00136	0.00429
k_{tot} (s^{-1}) (TCSPC)	2.05×10^{10}	1.64×10^{10}	9.47×10^{9}
k_r (s^{-1}) (TCSPC)	2.76×10^{7}	2.23×10^{7}	4.06×10^{7}
k_{nr} (s^{-1}) (TCSPC)	2.05×10^{10}	1.64×10^{10}	9.43×10^{9}
k_{tot} (s^{-1}) (TA)	3.13×10^{10}	2.01×10^{10}	9.17×10^{9}
k_r (s^{-1}) (TA)	4.23×10^{7}	2.73×10^{7}	3.94×10^{7}
k_{nr} (s^{-1}) (TA)	3.13×10^{10}	2.01×10^{10}	9.13×10^{9}
τ_{TCSPC} (ps)	48.9	61.0	105.6
τ_{TA} (ps)	31.9	49.8	109.0
τ_r (ns) (TCSPC)	36.2	44.8	24.6
τ_r (ns) (TA)	23.6	36.6	25.4
$\Delta\tau_r$ (ns)	12.6	8.2	0.8
exp. λ_{Abs} (nm)	1042	1044	1023
th. $\lambda_{Abs,S}$ (nm)	1043	1056	1072
th. $\lambda_{Abs,T}$ (nm)	1027	1071	1100
exp. λ_{Em} (nm)	1194	1202	1187
f_{exp}	0.58	0.47	0.86
th. $\lambda_{Em,S}$ (nm)	1130	1147	1163

[a]All measurements were taken in DCM at 298 K. See Methods for details and equations used in the determination of radiative rates and lifetimes. Th. and exp. indicate theoretically and experimentally obtained values, respectively. S and T indicate singlet and triplet transitions, respectively.

absorption (ESA) at 1100 nm growing in shortly thereafter (Figure 1c,d). A feature at ∼1200 nm grows in at a similar rate to the ESA. We assign this as a stimulated emission (SE), and the similar lifetime of the SE and ESA suggests they correspond to the population of a single excited state.

These three features are consistent across all complexes, suggesting a similar electronic structure despite modification of capping metals and ligands. However, we do note variations at longer timepoints (∼ns, see the Supporting Information). For example, both **2** and **3** exhibit the growth of a low-energy ESA at ∼1350 nm that is notably absent in the TA spectrum of **1**. This feature is potentially indicative of intersystem crossing, although additional data will need to be acquired to confirm this assignment.

There is moderate variation in the excited-state lifetimes across **1**, **2**, and **3**, ranging from ∼31−109 ps (see Figure 1e and Table 1). These lifetimes were compared to the PL decay acquired via a time-correlated single-photon counting (TCSPC) system. The TCSPC lifetimes (see the Supporting Information) are remarkably consistent with the SE assignment of the ∼1200 nm TA feature. Furthermore, measurement under both aerobic and anaerobic conditions showed no significant changes (Figure 1e, inset). The similarity of the aerobic and anaerobic decays strongly indicates fluorescence from a singlet excited state.

We then used the lifetimes and PLQY values to determine the radiative rates and lifetimes for each complex (see the Experimental Section and Supporting Information). There is minimal variation between TA- and TCSPC-derived lifetimes. As expected for NIR II transitions, the nonradiative lifetimes for all three analogues are quite short at 10^{-10} to 10^{-9} seconds (see Table 1); however, these values are long compared to many organic systems emitting past 1100 nm.[40] We propose that the comparatively long nonradiative lifetimes arise from

https://doi.org/10.1021/jacs.2c04976
J. Am. Chem. Soc. 2022, 144, 16447−16455

weak electronic coupling and/or a small reorganization energy associated with the relaxation process (see the Experimental Section and Supporting Information). Overall, the brighter emission may be enabled by a lack of higher frequency vibrations (i.e., C−H's) in the TTFtt core, where absorption and emission are localized. In tandem, the radiative lifetimes for **1**, **2**, and **3** are ∼35 ns, which are consistent with $\pi-\pi$ transitions.[40] The experimentally determined lifetimes enable the calculation of oscillator strengths which range from 0.47 to 0.86. These values are high, comparable with the best molecular lumiphores, further explaining the bright emission from these complexes.[38]

Electronic Structure. Previous studies suggest that singlet and triplet states are close in energy in TTFtt dicationic complexes.[31,41] Consistent with this hypothesis, the ^{1}H NMR spectra of **1**, **2**, and **3** appear diamagnetic; however, there is a significant magnetic moment detected via Evans method measurements for all three complexes (see the Supporting Information). Furthermore, a strong signal at $g = 2$ suggestive of an organic radical is present in the electron paramagnetic resonance (EPR) spectra of these complexes (see the Supporting Information).[42] Variable temperature measurements (see the Supporting Information) show this signal near $g = 2$ growing in intensity as temperature is increased, suggesting a singlet ground state with thermal population of a triplet excited state.

These experimental findings were further supported by complete active space self-consistent field (CASSCF) calculations using the variational two-electron reduced density matrix (V2RDM) method[43,44] in the Maple Quantum Chemistry Package.[45,46] An active space encompassing 20 electrons distributed in 20 spatial orbitals, [20, 20], was utilized in combination with the 6-31G basis set for all atoms but Pd and Pt, which were treated with the LANL2TZ basis set and effective core potential (ECP).[47−49] The active space initial guess was selected using MP2 natural orbitals, which were subsequently optimized via CASSCF orbital rotations.

Our calculations reveal all complexes to exhibit open-shell singlet ground states with significant degrees of multireference correlation and biradical character, in line with previous studies on related TTFtt systems.[31,32] The triplet-singlet gaps obtained with V2RDM and density functional theory (DFT) increase across the series **2** < **1** < **3** as the degree of fractional occupation in the highest occupied natural orbital (HONO) and lowest unoccupied natural orbital (LUNO) decreases from $\eta_{LUNO,S} = 0.46$, $\eta_{HONO,S} = 1.57$ in **2** to $\eta_{LUNO,S} = 0.33$, and $\eta_{HONO,S} = 1.72$ in **3**. Inspection of the frontier natural-orbital densities reveals that the multireference correlation arises from near-degeneracy of the HONO and LUNO, which have A_g and A_u symmetries and are π^*-antibonding and π-bonding across the central TTFtt C−C bond, respectively. The CASSCF result contains a mixture of both ligand- and metal-centered NOs; however, the strongly correlated orbitals are nearly exclusively localized on the TTFtt core, with little contribution from the metal-based orbitals (see the Supporting Information).

Time-dependent DFT (TD-DFT)[50] calculations were performed to elucidate the electronic processes underlying the observed luminescent behavior. Ground-state geometries were first relaxed from the crystal structures using DFT and then followed by TD-DFT calculations. The electronic emission spectra were modeled by performing TD-DFT geometry optimizations on the A_u excited states. All calculations used the PBE0 functional[51] as implemented in Gaussian 16[52] in combination with the LANL2DZ basis set[53] with an ECP for Pt and Pd, and the 6-31G* basis set for all other atoms, and the SMD solvation model.[54]

Calculations yield excellent agreement with experimental absorption data (Table 1, see the Supporting Information); deviations from spectroscopic measurements are low and range from 1 nm in **1** to 49 nm in **3**. Due to the relatively small singlet−triplet gap in both V2RDM and B3LYP[55] calculations, we calculated transitions from a triplet ground state in addition to those from the broken-symmetry singlet. The $T_1 \rightarrow T_2$ transitions are near degenerate with the singlet transitions in all three complexes, albeit with slightly lower oscillator strengths.

In addition, the modeled emission spectra yielded excellent agreement with the experimentally measured PL spectra. The transitions and natural transition orbitals are summarized in the Jablonski diagram for **2** (Figure 2). Interestingly, the orbital

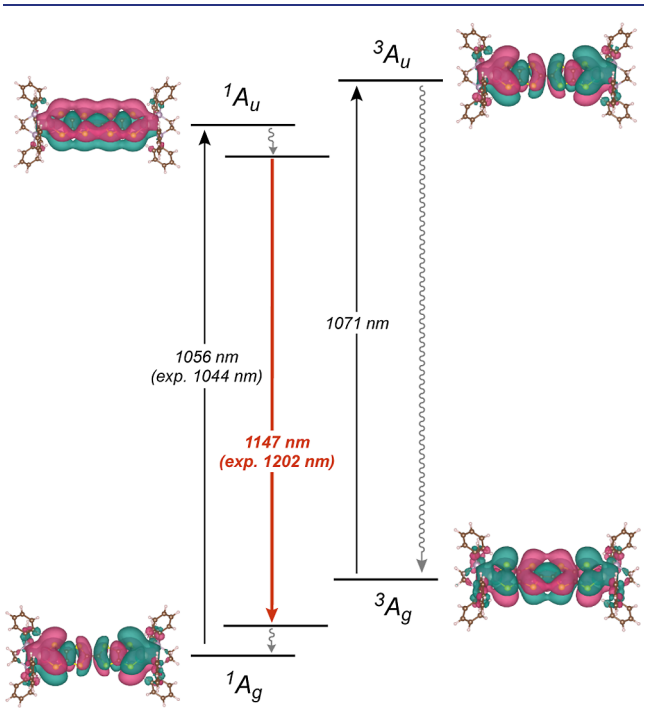

Figure 2. Electronic structure of TTFtt dications. Jablonski diagram of **2** showing absorption and emission of singlet states. Calculated triplet absorption is shown relative in energy to the calculated singlet transitions.

character is almost entirely based on the TTFtt unit, suggesting that many different end caps can be included and modified for targeting, switching, stability, or solubility.

Stable and Switchable Fluorescence. Many applications of NIR lumiphores require water compatibility or solubility. We therefore measured absorption and emission in 1:1 MeCN/H_2O. We note a hypsochromic shift of these features in 1:1 MeCN/H_2O compared with dichloromethane (DCM), and studies across a range of solvents support a negative solvatochromic trend (see the Supporting Information). While **1**−**3** display somewhat reduced stability in this solvent mixture due to partial reduction, the complexes still emit quite brightly (Figure 3a). This bright emission is notable even with the presence of strong water absorptions at ∼1200−1400 nm. PLQY values for **2** and **3** were obtained in this mixture and, remarkably, **3** has a PLQY of 0.08%, nearly double that of IR

https://doi.org/10.1021/jacs.2c04976
J. Am. Chem. Soc. 2022, 144, 16447−16455

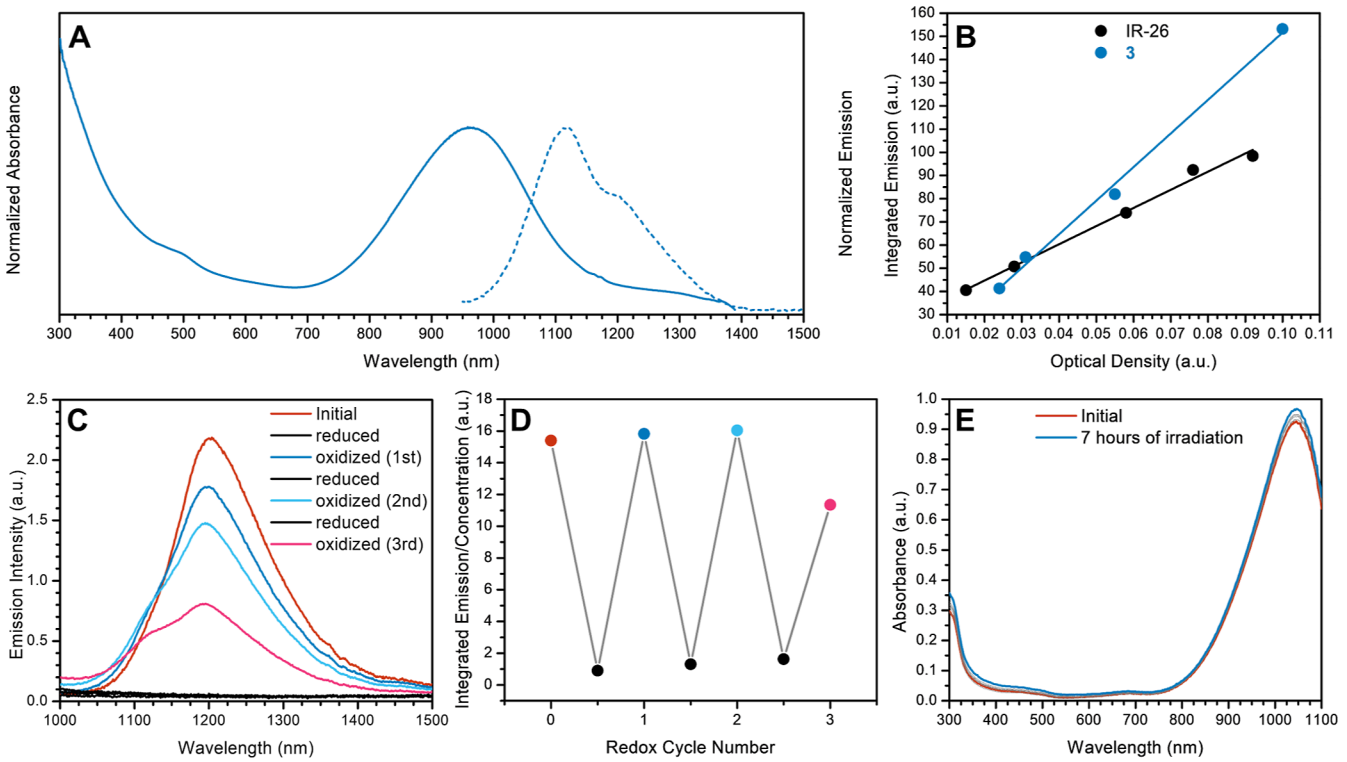

Figure 3. Stability, redox switchable behavior, and aqueous emission. (a) Normalized UV−vis−NIR and PL spectra of **3** in 1:1 MeCN/H_2O. (b) PLQY determination of **3** in 1:1 MeCN/H_2O using IR 26 in 1,2-dichloroethane as a reference. Optical density was measured at the excitation wavelength (900 nm) for both samples. (c) PL intensity upon reduction and oxidation of **2** in DCM across multiple redox cycles. The shoulder apparent at low concentrations can be attributed to DCM absorptions. (d) Integrated emission of **2** in DCM across multiple redox cycles after normalization for concentration. (e) UV−vis spectra of **2** in DCM under continuous irradiation of a 940 nm light-emitting diode (LED).

26 in 1,2-dichloroethane (Figure 3b).[27] Complex **2** has a moderately reduced PLQY of 0.04% in the aqueous mixture but is significantly more stable (see the Supporting Information). These examples illustrate that minor capping metal and ligand adjustments enable modification of both redox stability and emission intensity.

The TTFtt-based luminescence reported here is unprecedented. Given this, we also investigated whether the monoreduced analogues of these complexes, with formal TTF radical cation cores, were luminescent. To test this, we injected a DCM solution of $CoCp_2$ into a sealed cuvette containing **2** in DCM to reduce the dicationic complex to its monocationic form in situ. No measurable emission was detected after this reduction (Figure 3c). To probe whether the fluorophore can be recovered, a DCM solution of $[Fc^{BzO}][BAr_4^F]$ was injected into the same cuvette. Bright emission was again detected, with a slight reduction in PL intensity that can be attributed to dilution of the sample. Two more redox cycles were carried out, with similar recovery of the original fluorescence intensity after correcting for concentration (Figure 3d). Given the quenching of all emission upon reduction, and the remarkable recovery of the original fluorophore upon reoxidation, these systems are impressive candidates for redox sensing applications, particularly since they emit in the tissue transparent window and remain bright in aqueous solutions.

To further probe the stability of these complexes, **2** was irradiated with a 3 mW 940 nm LED. After 7 h of continuous irradiation, no significant changes or bleaching were apparent in the UV−vis spectrum that might indicate decomposition or reaction under this prolonged irradiation (Figure 3e). Furthermore, all three samples exhibited stability when exposed to 808 nm and 950 nm lasers when measuring PLQY values and TA spectra, respectively. Thus, we can conclude this family of complexes is remarkably photostable to NIR irradiation.

CONCLUSIONS

We have reported three novel TTFtt diradicaloid complexes that exhibit extraordinarily bright and modular fluorescent behavior. This family of complexes marks the first report of TTFtt-based luminescence, and the brightness and emission energy of these complexes distinguish them as an exciting new class of NIR II fluorophores. The compressed TTFtt π manifold allows for strong absorptions and bright emission far into the NIR II region without the need for the extended conjugation typically present in organic NIR dyes and lumiphores.

Additionally, these complexes are a unique example of air- and water-stable organic diradicaloids. The modulation of diradical behavior through the alteration of capping metal−ligand combinations allows for electronic structure modification and may enable the rational design of novel lumiphores.

Finally, the remarkable photostability and redox switchable behavior presented here provide a promising platform for a wide array of applications. The aforementioned redox tunability and bright NIR II emission suggest this novel class of NIR fluorophores has significant potential to advance imaging and sensing technologies.

https://doi.org/10.1021/jacs.2c04976
J. Am. Chem. Soc. 2022, 144, 16447−16455

EXPERIMENTAL SECTION

General Synthetic Methods. All transmetalation and oxidation reactions were performed under inert conditions (dry N_2) in an MBraun UNIlab glovebox. Elemental analyses (C, H, and N) were performed by Midwest Microlabs. All solvents were dried and purged with N_2 on a Pure Process Technology solvent system and subsequently filtered through activated alumina and stored over 4 Å molecular sieves. $TTFtt(SnBu_2)_2$,[32] $dppePtCl_2$,[56] $[Fc^{BzO}][BAr_4^F]$,[32] and $Pt(P(4\text{-}CF_3Ph)_3)_2Cl_2$[57] were prepared according to literature procedures. All other chemicals and reagents were purchased from commercial sources and used as received.

Synthesis and Characterization of ***1****.* $TTFtt(SnBu_2)_2$ (0.017 g, 0.022 mmol) was dissolved in 3 mL of DCM and slowly added to a suspension of $Pd(dppe)_2Cl_2$ (0.025 g, 0.043 mmol) in 3 mL of DCM. The light yellow suspension formed a shiny dark pink suspension upon addition of the orange solution of $TTFtt(SnBu_2)_2$ and was left to stir for 10 min. Next, $[Fc^{BzO}][BAr_4^F]$ (0.053 g, 0.046 mmol) was dissolved in 2 mL of DCM and slowly added to the stirring reaction. The dark pink suspension turned olive green upon addition of $[Fc^{BzO}][BAr_4^F]$ and was left to stir for 5 min. The solution was condensed to 1 mL under vacuum, and petroleum ether (5 mL) was slowly added to further precipitate out the final product. The solids were washed with petroleum ether several times (3 × 5 mL) and dried under vacuum. The crude product was redissolved in 1 mL of DCM, filtered through celite, and layered with petroleum ether. The layered solution was cooled to −35 °C and left to crystallize overnight. The resulting olive green crystals were collected and dried (0.051 g, 76.9% yield). Crystals suitable for SXRD were selected from a 1,2-dichloroethane/petroleum ether slow diffusion gradient left to crystallize over a 2 day period at −35 °C. ^1H NMR (400 MHz, CD_2Cl_2, 298 K): δ 2.69 (d, dppe), 7.55 (s, $[BAr_4^F]^-$), 7.56−7.58 (m, dppe), 7.63−7.69 (m, dppe), and 7.72 (s, $[BAr_4^F]^-$). $^{31}P\{^1H\}$ NMR (162 MHz, CD_2Cl_2, 298 K): δ 62.00. Anal. calcd for **1**, $C_{122}H_{72}B_2F_{48}Pd_2P_4S_8$: C 47.81%, H 2.37%, and N 0%; found: C 47.45%, H 2.49%, and N none.

Synthesis and Characterization of ***2****.* $TTFtt(SnBu_2)_2$ (0.042 g, 0.053 mmol) was dissolved in 3 mL of DCM and slowly added to a suspension of $Pt(dppe)_2Cl_2$ (0.070 g, 0.105 mmol) in 4 mL of DCM. The white suspension formed a shiny pink suspension upon addition of $TTFtt(SnBu_2)_2$ and was left to stir for 10 min. Next, $[Fc^{BzO}][BAr_4^F]$ (0.122 g, 0.105 mmol) was dissolved in 4 mL of DCM and slowly added to the stirring reaction. The shiny pink suspension turned green upon addition of $[Fc^{BzO}][BAr_4^F]$ and was left to stir for 5 min. The solution was condensed to 1 mL under vacuum, and petroleum ether (5 mL) was slowly added to further precipitate out the final product. The solids were washed with petroleum ether several times (3 × 5 mL) and dried under vacuum. The crude product was redissolved in 1 mL of DCM, filtered through celite, and layered with petroleum ether. The layered solution was cooled to −35 °C and left to crystallize overnight. The resulting dark green crystals were collected and dried (0.152 g, 88.9% yield). Crystals suitable for SXRD were selected from a 1,2-dichloroethane/pentane slow diffusion gradient left to crystallize over a 2 day period at −35 °C. ^1H NMR (400 MHz, CD_2Cl_2, 298 K): δ 2.62 (d, dppe), 7.55 (s, $[BAr_4^F]^-$), 7.57−7.62 (m, dppe), 7.64−7.70 (m, dppe), and 7.72 (s, $[BAr_4^F]^-$). $^{31}P\{^1H\}$ NMR (162 MHz, CD_2Cl_2, 298 K): δ 47.09 ($J_{Pt,P}$ = 2919 Hz). $^{195}Pt\{^1H\}$ NMR (107 MHz, CD_2Cl_2, 298 K): δ −4597.51. Anal. calcd for **2**, $C_{122}H_{72}B_2F_{48}Pt_2P_4S_8$: C 45.19%, H 2.24%, N 0%; found: C 45.31%, H 2.59%, and N none.

Synthesis and Characterization of ***3****.* $TTFtt(SnBu_2)_2$ (0.023 g, 0.029 mmol) was dissolved in 3 mL of DCM and slowly added to a solution of $Pt(P(4\text{-}CF_3Ph)_3)_2Cl_2$ (0.070 g, 0.058 mmol) in 3 mL of DCM. The colorless solution turned dark brown upon addition of $TTFtt(SnBu_2)_2$ and was left to stir for 5 min. Next, $[Fc^{BzO}][BAr_4^F]$ (0.067 g, 0.058 mmol) was dissolved in 2 mL of DCM and slowly added to the stirring reaction. The dark brown solution turned green upon addition of $[Fc^{BzO}][BAr_4^F]$ and began to crystallize out of solution. The solution was condensed to 1 mL under vacuum, and petroleum ether (5 mL) was slowly added to further precipitate out the final product. The solids were washed with petroleum ether several times (3 × 5 mL) and dried under vacuum. The crude product was redissolved in 1 mL of DCM, filtered through celite, and layered with petroleum ether. The layered solution was cooled to −35 °C and left to crystallize overnight. The resulting blue-green crystals were collected and dried (0.089 g, 70.7% yield). Crystals suitable for SXRD were selected from a DCM/petroleum ether slow diffusion gradient left to crystallize over a 2 day period at −35 °C. ^1H NMR (400 MHz, CD_2Cl_2, 298 K): δ 7.48 (s, $[BAr_4^F]^-$), 7.51 (d, $PhCF_3$), 7.62 (d, $PhCF_3$), and 7.70 (s, $[BAr_4^F]^-$). $^{31}P\{^1H\}$ NMR (202 MHz, CD_2Cl_2, 298 K): δ 14.92 ($J_{Pt,P}$ = 2992 Hz). $^{195}Pt\{^1H\}$ NMR (107 MHz, CD_2Cl_2, 298 K): δ −4490.87. Anal. calc. for **3**, $C_{154}H_{72}B_2F_{84}Pt_2P_4S_8$: C 42.91%, H 1.69%, N 0%; found: C 42.36%, H 1.87%, and N none.

Characterization and Analysis Methods. *Single-Crystal X-ray Diffraction.* All SXRD data were acquired at 100 K on a Bruker D8 VENTURE diffractometer equipped with a microfocus Mo-target X-ray tube (λ = 0.71073 Å) and a PHOTON 100 CMOS detector. Single crystals were mounted on a cryo-loop and transferred into the diffractometer nitrogen stream prior to collection. Data reduction and integration were performed with the Bruker APEX3[58] software package (Bruker AXS, version 2015.5-2, 2015). Data were scaled and corrected for absorption effects using the multiscan procedure as implemented in SADABS (Bruker AXS, version 2014/54, 2015). All crystal structures were solved by SHELXT[59] (version 2014/55) and refined by a full-matrix least-squares procedure using OLEX26[60] (XL refinement program version 2018/17). Disorder was modeled with common restraints.

Cyclic Voltammetry. Cyclic voltammetry measurements were performed using a glassy carbon working electrode, a silver wire pseudoreference, and a platinum wire counter electrode. Each voltammogram was referenced to internal $FcCp_2^+/FcCp_2$. All measurements were acquired using a BAS Epsilon potentiostat and analyzed using the BASi Epsilon software version 1.40.67NT.

EPR Spectroscopy. EPR measurements were conducted on a Bruker Elexsys E500 spectrometer equipped with a Bruker Cold-Edge stinger and an Oxford ESR 900 X-band cryostat.

Fourier Transform Infrared Spectroscopy. All IR measurements were performed by dropcasting DCM solutions onto KBr plates. Each spectrum was acquired on a Bruker Tensor II; both background subtractions and baseline corrections were applied for each complex using the OPUS software.

NMR Spectroscopy. ^1H, ^{31}P, and ^{195}Pt NMR spectra were acquired on Bruker DRX 400 and 500 spectrometers. Residual solvent peaks were referenced for all ^1H NMR measurements, and 85% phosphoric acid and sodium hexachloroplatinate were used as references for ^{31}P and ^{195}Pt NMR measurements, respectively. Evans method measurements were all conducted in CD_2Cl_2 with a capillary insert of 95/5 w/w % CD_2Cl_2/DCM. Pascal's constants were used to correct for the diamagnetic contribution of each complex.[61]

UV−Vis−NIR Spectroscopy. UV−vis−NIR measurements were performed using a Shimadzu UV-3600 Plus dual-beam spectrophotometer. UV−vis region spectra were acquired on a Thermo Scientific Evolution 300 spectrometer with the VISIONpro software suite. Variable-temperature measurements were performed using a Unisoku CoolSpeK 203-B cryostat.

PL Spectroscopy. All emission spectra were acquired on a Horiba Scientific PTI QuantaMaster fluorometer. Low-temperature emission spectra were recorded by adding samples in 1:1 DCM/toluene into quartz EPR tubes and lowering the tube into an optical dewar filled with liquid N_2. Excitation emission matrices were acquired on a HORIBA Scientific Fluorolog-3 spectrofluorometer.

TA Spectroscopy. TA spectroscopy was performed using a 5 kHz amplified titanium/sapphire laser with a 120fs laser pulsewidth. A portion of the 800 nm fundamental output was focused into a sapphire crystal to produce NIR continuum probe pulses that were mechanically delayed. Pump pulses were tuned to 950 nm using an optical parametric amplifier, and a mechanical chopper reduced the repetition rate to 2.5 kHz. Samples were stirred during experiments and excited with 0.2 mW of pump power.

https://doi.org/10.1021/jacs.2c04976
J. Am. Chem. Soc. 2022, 144, 16447−16455

Lifetime Measurements. TCSPC was performed on the samples using a 975 nm diode laser with a 60 ps pulsewidth operating at 20 MHz. Collected PL was dispersed using a 0.3 m spectrograph and detected with a superconducting nanowire single-photon detector and a multichannel scaler with 25 ps bin width.

PL Quantum Yield Determination. The samples, sealed in NMR tubes, were individually placed in an integrating sphere (Thorlabs, IS200-4) with a PbSe detector (Thorlabs, PDA20H) on one port and directly excited by an 808 nm diode laser (Thorlabs, M9-808-0150) of 15 W/cm^2 average intensity under 1 kHz square-wave modulation. The detector signal S, with and without a silicon window on the detector port, was recorded with the sample and with a DCM blank. 808 nm light is completely blocked by the silicon window within the sensitivity of the measurement. The PLQY is therefore

$$\phi = S_{S,Si}/T(S_D - S_S)$$

where the subscripts S, D, and Si, respectively, denote the sample, DCM blank, and silicon window. T is the total normalized emission signal transmitted by the silicon window. Due to the spectral overlap between the sample emission and the soft absorption edge of silicon, we calculate T explicitly as

$$\int E(\lambda)\mathrm{d}\lambda \times \left(\int \frac{E(\lambda)}{T(\lambda)} \right)^{-1}$$

where $E(\lambda)$ is the normalized sample emission spectrum and $T(\lambda)$ is the normalized silicon window transmission spectrum.

Radiative Rate and Oscillator Strength Determination. The experimental oscillator strength values were determined using the experimentally determined quantum yield values, ϕ, and the TCSPC PL lifetimes. Both values were utilized to determine the radiative rate through the expression $\phi = k_r/(k_r + k_{nr})$, where the denominator, $(k_r + k_{nr})$, is the reciprocal of the PL lifetime, τ_{TCSPC}. We then obtained the oscillator strength, f, which is related to the radiative rate by

$$f = \frac{k_r mc^3}{2\omega^2 e^2 F} \times \frac{g_1}{g_2}$$

where m is the free electron mass, c is the vacuum speed of light, e is the electron charge, ω is the angular frequency of the light, and g_1 and g_2 are degeneracies of the upper (2) and lower (1) states involved in the optical transition, respectively, the ratio of which we assumed to be 1.[62] The factor $F = \sqrt{\varepsilon} \times (3\varepsilon/(2\varepsilon + 1))^2$ accounts for the radiation density of states and local field screening in a matrix of optical dielectric constant ε, where $\varepsilon = 2$ for DCM.[63,64]

Energy Gap Law Calculations and Discussion. Given the relatively small Stokes shift of ∼1400 cm^{-1}, we interpreted the PL efficiency within the weak-coupling gap law regime presented by Englman and Jortner.[15,17] In this case, when k_BT is smaller than the energy of the highest-frequency fundamental vibrational mode, Englman and Jortner proposed the nonradiative rate to be

$$k_{nr} = \frac{J^2}{\hbar}\sqrt{\frac{2\pi}{\hbar\omega_M \Delta E}} \exp\left(-\left(\ln\left(\frac{\Delta E}{de_M} \right) - 1 \right) \frac{\Delta E}{\hbar\omega_M} \right)$$

The exponential factor is related to the Franck−Condon factors for the vibrations of the ground electronic state, and J is an effective nonadiabatic electronic coupling between ground and excited electronic states ($J/hc \sim 100$−700 cm^{-1} for polycyclic organics[15]). ω_M is the frequency of the highest-frequency fundamental vibration ($\omega_M/2\pi c = 2900$ cm^{-1} for C−H stretches), ΔE is the vertical absorption energy (absorption maximum for weak coupling, ∼10 000 cm^{-1}), $2e_M$ is the portion of the Stokes shift that arises from the highest-frequency modes ($2e_M/hc \leq 1400$ cm^{-1}), and d is the number of vibrational modes at ω_M that are active in the relaxation. In an analogy to Marcus-type models, the product de_M may be thought of as a reorganization energy associated with the relaxation process. Although d, e_M, and J might ultimately be obtainable from detailed simulations, they are taken here as constrained adjustable parameters.

■ ASSOCIATED CONTENT

Supporting Information

The Supporting Information is available free of charge at https://pubs.acs.org/doi/10.1021/jacs.2c04976.

Detailed experimental and computational procedures and additional spectra (PDF)

Accession Codes

CCDC 2171695−2171697 contain the supplementary crystallographic data for this paper. These data can be obtained free of charge via www.ccdc.cam.ac.uk/data_request/cif, or by emailing data_request@ccdc.cam.ac.uk, or by contacting The Cambridge Crystallographic Data Centre, 12 Union Road, Cambridge CB2 1EZ, UK; fax: +44 1223 336033.

■ AUTHOR INFORMATION

Corresponding Author

John S. Anderson − *Department of Chemistry, The University of Chicago, Chicago, Illinois 60637, United States;* orcid.org/0000-0002-0730-3018; Email: jsanderson@uchicago.edu

Authors

Lauren E. McNamara − *Department of Chemistry, The University of Chicago, Chicago, Illinois 60637, United States;* orcid.org/0000-0002-1169-8171

Jan-Niklas Boyn − *Department of Chemistry, The University of Chicago, Chicago, Illinois 60637, United States;* orcid.org/0000-0002-6240-3759

Christopher Melnychuk − *Department of Chemistry, The University of Chicago, Chicago, Illinois 60637, United States;* orcid.org/0000-0003-4503-4135

Sophie W. Anferov − *Department of Chemistry, The University of Chicago, Chicago, Illinois 60637, United States;* orcid.org/0000-0003-3972-5845

David A. Mazziotti − *Department of Chemistry, The University of Chicago, Chicago, Illinois 60637, United States;* orcid.org/0000-0002-9938-3886

Richard D. Schaller − *Center for Nanoscale Materials, Argonne National Laboratory, Argonne, Illinois 60439, United States; Department of Chemistry, Northwestern University, Evanston, Illinois 60208, United States*

Complete contact information is available at: https://pubs.acs.org/10.1021/jacs.2c04976

Notes

The authors declare no competing financial interest.

■ ACKNOWLEDGMENTS

Part of this work was performed at the Soft Matter Characterization Facility at the Pritzker School of Molecular Engineering at the University of Chicago. J.S.A. and D.A.M. gratefully acknowledge support for this work from the U.S. Department of Energy, Office of Science, Office of Basic Energy Sciences, under the grant DE-SC0019215. J.S.A. also gratefully acknowledges support from the 3M corporation through an NTFA, the Army Research Office under the grant W911NF-20-1-0091, and from a Dreyfus Teacher-Scholar Award (TC-21-064). This work was supported by the Chicago MRSEC, which is funded by NSF through the grant DMR-1420709. D.A.M. also gratefully acknowledges support from the ACS Petroleum Research Fund grant no. PRF no. 61644-ND6 and the U. S. National Science Foundation grant no.

CHE-1565638. This work was performed, in part, at the Center for Nanoscale Materials, a DOE Office of Science User Facility, and supported by the U.S. Department of Energy, Office of Science, Office of Basic Energy Sciences under contract no. DE-AC02-06CH11357. Jiaze Xie, Libai Huang, Galina Grechishnikova, and Sarath Santhakumar are thanked for helpful discussions.

REFERENCES

(1) Hong, G.; Antaris, A. L.; Dai, H. Near-Infrared Fluorophores for Biomedical Imaging. *Nat. Biomed. Eng.* **2017**, *1*, 0010.
(2) Matsui, A.; Tanaka, E.; Choi, H. S.; Winer, J. H.; Kianzad, V.; Gioux, S.; Laurence, R. G.; Frangioni, J. V. Real-Time Intra-Operative Near-Infrared Fluorescence Identification of the Extrahepatic Bile Ducts Using Clinically Available Contrast Agents. *Surgery* **2010**, *148*, 87−95.
(3) Li, B.; Zhao, M.; Feng, L.; Dou, C.; Ding, S.; Zhou, G.; Lu, L.; Zhang, H.; Chen, F.; Li, X.; Li, G.; Zhao, S.; Jiang, C.; Wang, Y.; Zhao, D.; Cheng, Y.; Zhang, F. Organic Nir-II Molecule with Long Blood Half-Life for in Vivo Dynamic Vascular Imaging. *Nat. Comm.* **2020**, *11*, 3102.
(4) Qu, C.; Xiao, Y.; Zhou, H.; Ding, B.; Li, A.; Lin, J.; Zeng, X.; Chen, H.; Qian, K.; Zhang, X.; Fang, W.; Wu, J.; Deng, Z.; Cheng, Z.; Hong, X. Quaternary Ammonium Salt Based NIR-II Probes for in Vivo Imaging. *Adv. Opt. Mater.* **2019**, *7*, 1900229.
(5) Zeng, X.; Xiao, Y.; Lin, J.; Li, S.; Zhou, H.; Nong, J.; Xu, G.; Wang, H.; Xu, F.; Wu, J.; Deng, Z.; Hong, X. Near-Infrared II Dye-Protein Complex for Biomedical Imaging and Imaging-Guided Photothermal Therapy. *Adv. Healthcare Mater.* **2018**, *7*, 1800589.
(6) Antaris, A. L.; Chen, H.; Diao, S.; Ma, Z.; Zhang, Z.; Zhu, S.; Wang, J.; Lozano, A. X.; Fan, Q.; Chew, L.; Zhu, M.; Cheng, K.; Hong, X.; Dai, H.; Cheng, Z. A high quantum yield molecule-protein complex fluorophore for near-infrared II imaging. *Nat. Comm.* **2017**, *8*, 15269.
(7) Wu, J.-J.; Wang, X.-D.; Liao, L.-S. Near-Infrared Solid-State Lasers Based on Small Organic Molecules. *ACS Photonics* **2019**, *6*, 2590−2599.
(8) Song, Y.; Yu, G.; Xie, B.; Zhang, K.; Huang, F. Visible-to-Near-Infrared Organic Photodiodes with Performance Comparable to Commercial Silicon-Based Detectors. *Appl. Phys. Lett.* **2020**, *117*, 093302.
(9) Ho, C.-L.; Li, H.; Wong, W.-Y. Red to near-Infrared Organometallic Phosphorescent Dyes for OLED Applications. *J. Organomet. Chem.* **2014**, *751*, 261−285.
(10) Zhang, R.; Xu, Y.; Zhang, Y.; Kim, H. S.; Sharma, A.; Gao, J.; Yang, G.; Kim, J. S.; Sun, Y. Rational Design of a Multifunctional Molecular Dye for Dual-Modal NIR-II/Photoacoustic Imaging and Photothermal Therapy. *Chem. Sci.* **2019**, *10*, 8348−8353.
(11) Sun, C.; Li, B.; Zhao, M.; Wang, S.; Lei, Z.; Lu, L.; Zhang, H.; Feng, L.; Dou, C.; Yin, D.; Xu, H.; Cheng, Y.; Zhang, F. J-Aggregates of Cyanine Dye for NIR-II in Vivo Dynamic Vascular Imaging Beyond 1500 nm. *J. Am. Chem. Soc.* **2019**, *141*, 19221−19225.
(12) Lei, Z.; Sun, C.; Pei, P.; Wang, S.; Li, D.; Zhang, X.; Zhang, F. Stable, Wavelength-Tunable Fluorescent Dyes in the NIR-II Region for in Vivo High-Contrast Bioimaging and Multiplexed Biosensing. *Angew. Chem.* **2019**, *131*, 8250−8255.
(13) Feng, Z.; Tang, T.; Wu, T.; Yu, X.; Zhang, Y.; Wang, M.; Zheng, J.; Ying, Y.; Chen, S.; Zhou, J.; Fan, X.; Zhang, D.; Li, S.; Zhang, M.; Qian, J. Perfecting and Extending the Near-Infrared Imaging Window. *Light: Sci. Appl.* **2021**, *10*, 197.
(14) Antaris, A. L.; Chen, H.; Cheng, K.; Sun, Y.; Hong, G.; Qu, C.; Diao, S.; Deng, Z.; Hu, X.; Zhang, B.; Zhang, X.; Yaghi, O. K.; Alamparambil, Z. R.; Hong, X.; Cheng, Z.; Dai, H. A Small-Molecule Dye for NIR-II Imaging. *Nat. Mater.* **2016**, *15*, 235−242.
(15) Yoon, S.; Teets, T. S. Red to near-Infrared Phosphorescent Ir (iii) Complexes with Electron-Rich Chelating Ligands. *Chem. Commun.* **2021**, *57*, 1975−1988.
(16) Lai, P.-N.; Yoon, S.; Teets, T. S. Efficient near-Infrared Luminescence from Bis-Cyclometalated Iridium (iii) Complexes with Rigid Quinoline-Derived Ancillary Ligands. *Chem. Commun.* **2020**, *56*, 8754−8757.
(17) Englman, R.; Jortner, J. The Energy Gap Law for Radiationless Transitions in Large Molecules. *Mol. Phys.* **1970**, *18*, 145−164.
(18) Lin, S. H. Energy Gap Law and Franck−Condon Factor in Radiationless Transitions. *J. Chem. Phys.* **1970**, *53*, 3766−3767.
(19) Troyan, S. L.; Kianzad, V.; Gibbs-Strauss, S. L.; Gioux, S.; Matsui, A.; Oketokoun, R.; Ngo, L.; Khamene, A.; Azar, F.; Frangioni, J. V. The Flare Intraoperative Near-Infrared Fluorescence Imaging System: A First-in-Human Clinical Trial in Breast Cancer Sentinel Lymph Node Mapping. *Ann. Surg Oncol.* **2009**, *16*, 2943−2952.
(20) Ashitate, Y.; Vooght, C. S.; Hutteman, M.; Oketokoun, R.; Choi, H. S.; Frangioni, J. V. Simultaneous Assessment of Luminal Integrity and Vascular Perfusion of the Gastrointestinal Tract Using Dual-Channel Near-Infrared Fluorescence. *Mol. Imaging* **2012**, *11*, 301−308.
(21) Tummers, Q. R. J. G.; Schepers, A.; Hamming, J. F.; Kievit, J.; Frangioni, J. V.; van de Velde, C. J. H.; Vahrmeijer, A. L. Intraoperative Guidance in Parathyroid Surgery Using Near-Infrared Fluorescence Imaging and Low-Dose Methylene Blue. *Surgery* **2015**, *158*, 1323−1330.
(22) Yang, Q.; Ma, H.; Liang, Y.; Dai, H. Rational Design of High Brightness NIR-II Organic Dyes with S-D-A-D-S Structure. *Acc. Mater. Res.* **2021**, *2*, 170−183.
(23) Yang, Q.; Hu, Z.; Zhu, S.; Ma, R.; Ma, H.; Ma, Z.; Wan, H.; Zhu, T.; Jiang, Z.; Liu, W.; Jiao, L.; Sun, H.; Liang, Y.; Dai, H. Donor Engineering for NIR-II Molecular Fluorophores with Enhanced Fluorescent Performance. *J. Am. Chem. Soc.* **2018**, *140*, 1715−1724.
(24) Ding, B.; Xiao, Y.; Zhou, H.; Zhang, X.; Qu, C.; Xu, F.; Deng, Z.; Cheng, Z.; Hong, X. Polymethine Thiopyrylium Fluorophores with Absorption Beyond 1000 nm for Biological Imaging in the Second Near-Infrared Subwindow. *J. Med. Chem.* **2018**, *62*, 2049−2059.
(25) Dou, K.; Feng, W.; Fan, C.; Cao, Y.; Xiang, Y.; Liu, Z. Flexible Designing Strategy to Construct Activatable NIR-II Fluorescent Probes with Emission Maxima Beyond 1200 nm. *Anal. Chem.* **2021**, *93*, 4006−4014.
(26) Fang, Y.; Shang, J.; Liu, D.; Shi, W.; Li, X.; Ma, H. Design, Synthesis, and Application of a Small Molecular NIR-II Fluorophore with Maximal Emission Beyond 1200 nm. *J. Am. Chem. Soc.* **2020**, *142*, 15271−15275.
(27) Semonin, O. E.; Johnson, J. C.; Luther, J. M.; Midgett, A. G.; Nozik, A. J.; Beard, M. C. Absolute Photoluminescence Quantum Yields of IR-26 Dye, PBS, and PbSe Quantum Dots. *J. Phys. Chem. Lett.* **2010**, *1*, 2445−2450.
(28) Stein, L.; Boden, P.; Naumann, R.; Förster, C.; Niedner-Schatteburg, G.; Heinze, K. The Overlooked NIR Luminescence of Cr(ppy)3. *Chem. Commun.* **2022**, *58*, 3701−3704.
(29) Boden, P.; Di Martino-Fumo, P.; Bens, T.; Steiger, S.; Albold, U.; Niedner-Schatteburg, G.; Gerhards, M.; Sarkar, B. NIR-Emissive Chromium (0), Molybdenum (0), and Tungsten (0) Complexes in the Solid State at Room Temperature. *Chem.—Eur. J.* **2021**, *27*, 12959−12964.
(30) Sinha, N.; Jiménez, J. R.; Pfund, B.; Prescimone, A.; Piguet, C.; Wenger, O. S. A Near-Infrared-II Emissive Chromium (III) Complex. *Angew. Chem., Int. Ed.* **2021**, *60*, 23722−23728.
(31) Kawamura, A.; Xie, J.; Boyn, J.-N.; Jesse, K. A.; McNeece, A. J.; Hill, E. A.; Collins, K. A.; Valdez-Moreira, J. A.; Filatov, A. S.; Kurutz, J. W.; Mazziotti, D. A.; Anderson, J. S. Reversible Switching of Organic Diradical Character via Iron-Based Spin-Crossover. *J. Am. Chem. Soc.* **2020**, *142*, 17670−17680.
(32) Xie, J.; Boyn, J.-N.; Filatov, A. S.; McNeece, A. J.; Mazziotti, D. A.; Anderson, J. S. Redox, Transmetalation, and Stacking Properties of Tetrathiafulvalene-2,3,6,7-Tetrathiolate Bridged Tin, Nickel, and Palladium Compounds. *Chem. Sci.* **2020**, *11*, 1066−1078.
(33) Gao, F.; Zhu, F.-F.; Wang, X.-Y.; Xu, Y.; Wang, X.-P.; Zuo, J.-L. Stabilizing Radical Cation and Dication of a Tetrathiafulvalene

Derivative by a Weakly Coordinating Anion. *Inorg. Chem.* **2014**, *53*, 5321−5327.
(34) McCullough, R. D.; Belot, J. A. Toward new magnetic, electronic, and optical materials: synthesis and characterization of new bimetallic tetrathiafulvalene tetrathiolate building blocks. *Chem. Mater.* **1994**, *6*, 1396−1403.
(35) McCullough, R. D.; Belot, J. A.; Rheingold, A. L.; Yap, G. P. Toward New Electronic, Magnetic, and Optical Materials: Structure and Properties of the First Homobimetallic Tetrathiafulvalene Tetrathiolate Building Block. *J. Am. Chem. Soc.* **1995**, *117*, 9913−9914.
(36) Bellec, N.; Vacher, A.; Barrière, F.; Xu, Z.; Roisnel, T.; Lorcy, D. Interplay between Organic−Organometallic Electrophores within Bis(Cyclopentadienyl)Molybdenum Dithiolene Tetrathiafulvalene Complexes. *Inorg. Chem.* **2015**, *54*, 5013−5020.
(37) Matsuo, Y.; Maruyama, M.; Gayathri, S. S.; Uchida, T.; Guldi, D. M.; Kishida, H.; Nakamura, A.; Nakamura, E. Π-Conjugated Multidonor/Acceptor Arrays of Fullerene−Cobaltadithiolene−Tetrathiafulvalene: From Synthesis and Structure to Electronic Interactions. *J. Am. Chem. Soc.* **2009**, *131*, 12643−12649.
(38) Bryce, M. R. Recent Progress on Conducting Organic Charge-Transfer Salts. *Chem. Soc. Rev.* **1991**, *20*, 355.
(39) Wang, H.-Y.; Cui, L.; Xie, J.-Z.; Leong, C. F.; D'Alessandro, D. M.; Zuo, J.-L. Functional Coordination Polymers Based on Redox-Active Tetrathiafulvalene and its Derivatives. *Coord. Chem. Rev.* **2017**, *345*, 342−361.
(40) Friedman, H. C.; Cosco, E. D.; Atallah, T. L.; Jia, S.; Sletten, E. M.; Caram, J. R. Establishing Design Principles for Emissive Organic SWIR Chromophores from Energy Gap Laws. *Chem* **2021**, *7*, 3359−3376.
(41) Boyn, J.-N.; McNamara, L. E.; Anderson, J. S.; Mazziotti, D. A. Interplay of Electronic and Geometric Structure Tunes Organic Biradical Character in Bimetallic Tetrathiafulvalene Tetrathiolate Complexes. *J. Phys. Chem. A* **2022**, *126*, 3329−3337.
(42) Abe, M. Diradicals. *Chem. Rev.* **2013**, *113*, 7011−7088.
(43) Gidofalvi, G.; Mazziotti, D. A. Active-Space Two-Electron Reduced-Density-Matrix Method: Complete Active-Space Calculations without Diagonalization of the N-Electron Hamiltonian. *J. Chem. Phys.* **2008**, *129*, 134108.
(44) Mazziotti, D. A. Large-Scale Semidefinite Programming for Many-Electron Quantum Mechanics. *Phys. Rev. Lett.* **2011**, *106*, 083001.
(45) Maplesoft, Maple, 2021. https://www.maplesoft.com (accessed Mar 3, 2022).
(46) Maplesoft, Quantum Chemistry Toolbox in Maple, 2021. https://www.maplesoft.com (accessed Mar 3, 2022).
(47) Francl, M. M.; Pietro, W. J.; Hehre, W. J.; Binkley, J. S.; Gordon, M. S.; DeFrees, D. J.; Pople, J. A. Self-Consistent Molecular Orbital Methods. XXIII. A Polarization-Type Basis Set for Second-Row Elements. *J. Chem. Phys.* **1982**, *77*, 3654−3665.
(48) Hehre, W. J.; Ditchfield, R.; Pople, J. A. Self—Consistent Molecular Orbital Methods. Xii. Further Extensions of Gaussian—Type Basis Sets for Use in Molecular Orbital Studies of Organic Molecules. *J. Chem. Phys.* **1972**, *56*, 2257−2261.
(49) Roy, L. E.; Hay, P. J.; Martin, R. L. Revised Basis Sets for the LANL Effective Core Potentials. *J. Chem. Theory Comput.* **2008**, *4*, 1029−1031.
(50) Bauernschmitt, R.; Ahlrichs, R. Treatment of Electronic Excitations within the Adiabatic Approximation of Time Dependent Density Functional Theory. *Chem. Phys. Lett.* **1996**, *256*, 454−464.
(51) Adamo, C.; Barone, V. Toward Reliable Density Functional Methods Without Adjustable Parameters: The PBE0 Model. *J. Chem. Phys.* **1999**, *110*, 6158−6170.
(52) Frisch, M. J.; Trucks, G. W.; Schlegel, H. B.; Scuseria, G. E.; Robb, M. A.; Cheeseman, J. R.; Scalmani, G.; Barone, V.; Petersson, G. A.; Nakatsuji, H.; Li, X.; Caricato, M.; Marenich, A. V.; Bloino, J.; Janesko, B. G.; Gomperts, R.; Mennucci, B.; Hratchian, H. P.; Ortiz, J. V.; Izmaylov, A. F.; Sonnenberg, J. L.; Williams-Young, D.; Ding, F.; Lipparini, F.; Egidi, F.; Goings, J.; Peng, B.; Petrone, A.; Henderson, T.; Ranasinghe, D.; Zakrzewski, V. G.; Gao, J.; Rega, N.; Zheng, G.; Liang, W.; Hada, M.; Ehara, M.; Toyota, K.; Fukuda, R.; Hasegawa, J.; Ishida, M.; Nakajima, T.; Honda, Y.; Kitao, O.; Nakai, H.; Vreven, T.; Throssell, K.; Montgomery, J. A., Jr.; Peralta, J. E.; Ogliaro, F.; Bearpark, M. J.; Heyd, J. J.; Brothers, E. N.; Kudin, K. N.; Staroverov, V. N.; Keith, T. A.; Kobayashi, R.; Normand, J.; Raghavachari, K.; Rendell, A. P.; Burant, J. C.; Iyengar, S. S.; Tomasi, J.; Cossi, M.; Millam, J. M.; Klene, M.; Adamo, C.; Cammi, R.; Ochterski, J. W.; Martin, R. L.; Morokuma, K.; Farkas, O.; Foresman, J. B.; Fox, D. J.. *Gaussian 16, Revision C.01*; Gaussian Inc.: Wallingford, Connecticut, 2016.
(53) Hay, P. J.; Wadt, W. R. Ab Initio Effective Core Potentials for Molecular Calculations. Potentials for the Transition Metal Atoms Sc to Hg. *J. Chem. Phys.* **1985**, *82*, 270−283.
(54) Marenich, A. V.; Cramer, C. J.; Truhlar, D. G. Universal Solvation Model Based on Solute Electron Density and on a Continuum Model of the Solvent Defined by the Bulk Dielectric Constant and Atomic Surface Tensions. *J. Phys. Chem. B* **2009**, *113*, 6378−6396.
(55) Becke, A. D. Density-Functional Thermochemistry. III. The Role of Exact Exchange. *J. Chem. Phys.* **1993**, *98*, 5648−5652.
(56) Burchell, C. J.; Aucott, S. M.; Milton, H. L.; Slawin, A. M.; Derek Woollins, J. Synthesis and characterisation of cyanodithioimidocarbonate [C2N2S2]2 complexes. *Dalton Trans.* **2004**, *3*, 369−374.
(57) Brune, H. A.; Falck, M.; Hemmer, R.; Schmidtberg, G. N.; Alt, H. G. Synthesen und spektroskopische untersuchungen substituierter cis - und trans -dichlorobis(triphenylphosphan)platin(ii)-verbindungen. *Chem. Ber.* **1984**, *117*, 2791−2802.
(58) Sheldrick, G. M. Crystal structure refinement with SHELXL. *Acta Crystallogr., Sect. C: Struct. Chem.* **2015**, *71*, 3−8.
(59) Sheldrick, G. M. SHELXT− integrated space-group and Crystal-structure determination. *Acta Crystallogr., Sect. A: Found. Adv.* **2015**, *71*, 3−8.
(60) Dolomanov, O. V.; Bourhis, L. J.; Gildea, R. J.; Howard, J. A.; Puschmann, H. Olex2: A complete structure solution, refinement and Analysis Program. *J. Appl. Crystallogr.* **2009**, *42*, 339−341.
(61) Bain, G. A.; Berry, J. F. Diamagnetic Corrections and Pascal's constants. *J. Chem.* **2008**, *85*, 532.
(62) Hilborn, R. C. Einstein coefficients, cross sections, f values, dipole moments, and all that. *Am. J. Physiol.* **1982**, *50*, 982.
(63) Onsager, L. Electric Moments of Molecules in Liquids. *J. Am. Chem. Soc.* **1936**, *58*, 1486.
(64) de Vries, P.; Lagendijk, A. Resonant scattering and spontaneous emission in dielectrics: Microscopic derivation of local-field effects. *Phys. Rev. Lett.* **1998**, *81*, 1381.

https://doi.org/10.1021/jacs.2c04976
J. Am. Chem. Soc. 2022, 144, 16447−16455